frontiers | Frontiers in Marine Science

TYPE Original Research
PUBLISHED 21 November 2022
DOI 10.3389/fmars.2022.1032699

OPEN ACCESS

EDITED BY
Arthur J. Miller,
University of California, San Diego,
United States

REVIEWED BY
Samiran Mandal,
Indian Institute of Technology Delhi,
India
Saikat Pramanik,
Indian National Centre for Ocean
Information Services, India

*CORRESPONDENCE
Anmin Zhang
anmin.zhang@tju.edu.cn

SPECIALTY SECTION
This article was submitted to
Physical Oceanography,
a section of the journal
Frontiers in Marine Science

RECEIVED 31 August 2022
ACCEPTED 20 October 2022
PUBLISHED 21 November 2022

CITATION
Sun C, Zhang A, Jin B, Wang X,
Zhang X and Zhang L (2022) Seasonal
variability of eddy kinetic energy in the
north Indian Ocean.
Front. Mar. Sci. 9:1032699.
doi: 10.3389/fmars.2022.1032699

Seasonal variability of eddy kinetic energy in the north Indian Ocean

Chunjian Sun[1,2], Anmin Zhang[1*], Baogang Jin[3], Xidong Wang[4], Xiaoshuang Zhang[2] and Lianxin Zhang[2]

[1]School of Marine Science and Technology, Tianjin University, Tianjin, China, [2]National Marine Data and Information Service, Tianjin, China, [3]Beijing Institute of Applied Meteorology, Beijing, China, [4]College of Oceanography, Hohai University, Nanjing, China

The seasonality of eddy kinetic energy (EKE) is analyzed in the north Indian Ocean by adopting high-resolution ocean reanalysis data. Significant eddy energy can be mainly spotted in six regions, including the Somali Current (SC) region, the Gulf of Aden, the Laccadive Sea, the east of Sri Lanka, the East Indian Coastal Current (EICC) region, and the northwest of Sumatra. As the most energetic region, the EKE averaged above 200 m could exceed 0.15 $m^2 \cdot s^{-2}$ in the SC region, whereas the mean EKE above 200 m is less than 0.04 $m^2 \cdot s^{-2}$ in the other regions. The barotropic and baroclinic instabilities are vital to eddy energy, and the contribution of each term in the barotropic/baroclinic equations varies with season and region. In the SC region and EICC region, EKE is primarily generated by barotropic conversion due to the sharp velocity shear caused by the strong SC during the summer monsoon and the EICC from March to June. For the other regions, the leading source of EKE is the eddy potential energy (EPE), which is extracted from available potential energy of mean flow *via* baroclinic conversion, and then the EPE is converted into EKE through vertical density flux. Once generated, EKE will be redistributed by pressure work and advection *via* eddy energy flux, which varies in sync with the monthly variation of total EKE, transporting EKE to the adjacent region or deeper layer. From the vertical aspect, eddy energy conversions are more prominent above 200 m. The maximal EKE and barotropic conversion mostly occur at the surface, whereas the EPE and baroclinic conversion may have two peaks, which lie at the surface and in the thermocline. Using the satellite altimeter data and wind data, we further investigate the impact of geostrophic eddy wind work, which reveals a slightly dampening effect to EKE in the north Indian Ocean.

KEYWORDS
mesoscale eddy, eddy kinetic energy, energy budget, north Indian Ocean, barotropic and baroclinic conversion

1 Introduction

The kinetic energy of eddy predominates in the global oceans, which is approximately one order of magnitude greater than the kinetic energy of mean current flows (Wyrtki et al., 1976; Richardson, 1983; Jia et al., 2011). As a vital part of ocean energy cascade, eddies exert great impacts on heat, salt, and mass transport through energy interactions with the mean flow (Stammer and Wunsch, 1999; Chelton et al., 2011a; Von Storch et al., 2012; Dong et al., 2014; Zhang et al., 2014; Qiu et al., 2021; Zhou et al., 2021). Therefore, understanding the eddy energy conversions is crucial. Previous studies reveal that the baroclinic/barotropic instabilities are the primary causes of energy transfer between eddy and mean flow (Gill et al., 1974; Ferrari and Wunsch, 2009; Venaille et al., 2011). The baroclinic/barotropic instabilities could induce forming and shedding of eddies. Conversely, eddies will feed back to mean flow as they propagate westward or shift into high-mode motions near the western boundary (Mata et al., 2006; Chelton et al., 2007; Zhai et al., 2010; Chelton et al., 2011b; Kuo and Chern, 2011). The eddy kinetic energy (EKE) can be produced by Reynolds interaction work *via* barotropic instability, whereas the eddy potential energy (EPE) can be generated by Ekman pumping through baroclinic instability (Eden and Böning, 2002; Zhai et al., 2008; Zu et al., 2022). From the spatial distribution, the energy exchange between eddy and mean flow is more intense in the strong current regions, since the sharp velocity shears and density gradients caused by the wind and current are capable of triggering baroclinic/barotropic conversions (Chen et al., 2014; Kang and Curchitser, 2015; Rieck et al., 2015). Temporally, the energy exchange is affected by seasonal variation of baroclinic/barotropic instability associated with the monsoonal wind and current (Qiu, 1999; Qiu and Chen, 2004; Uchida et al., 2017). Thus, investigating the spatial and temporal characteristics of eddy energy exchange is essential to understand the ocean energy budget.

Modulated by the inverted wind and currents (Figure 1), the eddy energy has distinct seasonal variation in the north Indian Ocean. In the Arabian Sea (AS), the Great Whirl (GW) generates under the driving of summer monsoon wind (Beal and Donohue, 2013; Vic et al., 2014), producing enormous EKE in the Somali Current (SC) region (Zhan et al., 2020). Then, the GW propagates northward and collides with Socotra Island, splitting into several small eddies and the Socotra Eddy (Fischer et al., 1996; Akuetevi et al., 2016). Meanwhile, branches of the SC cross Socotra Island from both sides, merging into the northward East Arabian Current (EAC), and bring the eddy energy northward (Fratantoni et al., 2006; Beal and Donohue, 2013). In the eastern AS, the cyclonic Laccadive Low emerges in the Laccadive Sea, which is induced by local and remote wind forcing (Bruce et al., 1994; Shankar and Shetye, 1997), while the anticyclonic Laccadive High takes its place in winter. As the SC and EAC reverse during the winter monsoon, their intensities also drop, producing less eddy energy than summer (Zhan et al., 2020). During this period, eddies may propagate into the Gulf of Aden under the driving of Rossby waves and southwestward EAC, thus enhancing the energy inside the gulf (Al Saafani et al., 2007). Compared to the monsoon stages, the eddy energy is

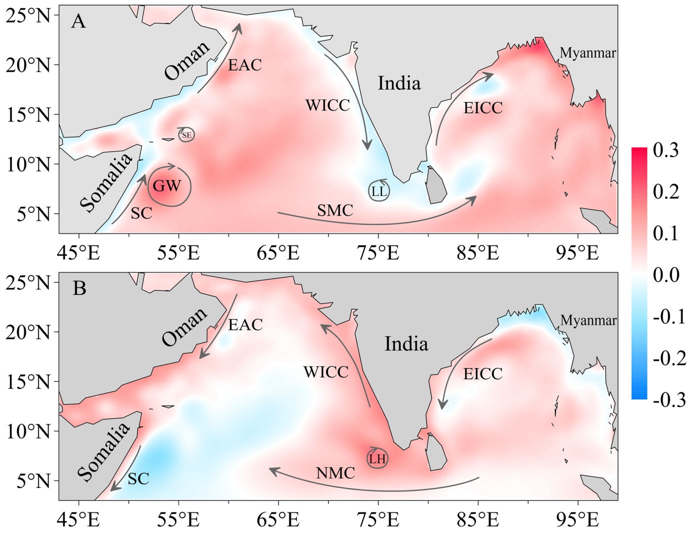

FIGURE 1
Schematic currents and eddies in the north Indian Ocean during the summer **(A)** and winter **(B)** monsoon. The abbreviations are as follows: SC, Somali Current; EAC, East Arabian Current; SMC, Southwest Monsoon Current; NMC, Northeast Monsoon Current; WICC, West India Coastal Current; EICC, East Indian Coastal Current; GW, Great Whirl; SE, Socotra Eddy; LH, Laccadive High; LL, Laccadive Low. The arrows show the direction of currents and the color shading represents the mean sea level anomaly from June to August **(A)** and from December to January **(B)** (unit: m).

weaker during the transitional phases due to unstable wind and current. For the Bay of Bengal (BOB), eddy activity is impacted by both seasonal and intraseasonal variabilities. During the summer monsoon, the Southwest Monsoon Current flows eastward at the south of Indian Peninsula (Schott and McCreary, 2001; Shankar et al., 2002), which interacts with the Sri Lankan coast and causes topographically trapped Rossby waves, subsequently, forming an anticyclonic eddy (AE) and a cyclonic eddy (CE) to the east of Sri Lanka (Pirro et al., 2020). Instead of the Southwest Monsoon Current, the westward Northeast Monsoon Current occurs in winter, amplifying the eddy energy around the south tip of India and Sri Lanka. Along the west boundary of BOB, the East Indian Coastal Current (EICC) flows northward (southward) from February (October) to September (January), elevating the eddy energy by strong velocity shears during these periods (Chen et al., 2012; Cheng et al., 2013). Moreover, the eddy energy is also remarkable at the northwest of Sumatra and the coastal rim of the BOB as well, which is affected by ocean internal instability, together with local wind stresses and intraseasonal oscillations from equatorial wind forcing (Chen et al., 2018). Moreover, the nonlinear processes caused by the coastline geometries of Myanmar bump and Andaman and Nicobar Islands considerably increase the eddy activity in the western and central parts of the BOB (Cheng et al., 2018; Mukherjee et al., 2019). As a result, the spatial and temporal characteristics of eddy energy are more complicated in the BOB.

To approach a comprehensive insight of seasonal EKE variabilities in the north Indian Ocean (the selected coverage is 3°–26°N, 43°–99°E), this study investigates the major eddy energy terms by adopting ocean reanalysis data and satellite data from 2000 to 2019. Six eddy-active regions in the AS and BOB are selected as the representative regions, and the regional averaged eddy energy terms are comparatively analyzed to quantify the monthly characteristics and vertical structures in the representative regions. Moreover, the four (two) terms in the barotropic (baroclinic) equation are calculated separately to probe into the monthly contribution of each term in detail. The remainder of this paper is organized as follows: Section 2 introduces the data and methods used in this paper. Section 3.1 describes the monthly variations of EKE and EPE. Section 3.2 evaluates the impacts of barotropic and baroclinic conversions. Section 3.3 explores the horizontal and vertical redistributions of eddy energy. The effect of wind work is discussed in Section 3.4. Eventually, the summary and discussion are given in Section 4.

2 Data and methods

2.1 Data

The eddy-resolving ocean reanalysis data of GLORYS12V1 is adopted in this study, which is produced by Mercator Ocean International and distributed by the Copernicus Marine Environment Monitoring Service (CMEMS). The reanalysis data is based on the global CMEMS forecasting system covering the satellite altimetry data since 1993, with a horizontal resolution of 1/12° and 50 vertical levels (Lellouche et al., 2018). This dataset has been used in numerous eddy studies, which is capable of reproducing the major mesoscale eddy features (de Marez et al., 2020; Verezemskaya et al., 2021; Yang et al., 2022). The sea level anomaly data and the surface geostrophic current data are obtained from the Archiving, Validation and Interpretation of Satellite Oceanographic data (Ducet et al., 2000). Additionally, the Cross-Calibrated Multi-Platform Version-2.0 wind data from the Remote Sensing Systems (Atlas et al., 2011; Wentz et al., 2015) is employed to analyze the wind stress work. The following study is based on the aforementioned data from 2000 to 2019 in order to get a statistical overview of the last two decades.

2.2 Eddy energy analysis methods

To evaluate the energy conversion between eddy and mean current flow, the four-box energy budget method is adopted in the study region (Lorenz, 1955; Böning and Budich, 1992). The equations are as follows:

$$\mathrm{EKE} = \frac{1}{2}(u'^2 + v'^2) \tag{1}$$

$$\mathrm{EPE} = -\frac{g\tilde{\rho}'^2}{2\rho(\partial\bar{\rho}_\theta/\partial z)} \tag{2}$$

$$\text{The barotropic conversion : T4}$$

$$= -\left(u'u'\frac{\partial\bar{u}}{\partial x} + u'v'\frac{\partial\bar{v}}{\partial x} + u'v'\frac{\partial\bar{u}}{\partial y} + v'v'\frac{\partial\bar{v}}{\partial y}\right) \tag{3}$$

$$\text{The baroclinic conversion : T2}$$

$$= -\frac{g}{-\rho(\partial\bar{\rho}_\theta/\partial z)}\left(u'\tilde{\rho}'\frac{\partial\bar{\tilde{\rho}}}{\partial x} + v'\tilde{\rho}'\frac{\partial\bar{\tilde{\rho}}}{\partial y}\right) \tag{4}$$

where $u' = u - \bar{u}$, $v' = v - \bar{v}$. To retain the intraseasonal signals of the ocean, $u^{'}$ and $v^{'}$ are the deviations from 101 days running mean of the current velocities ($\bar{u}$ and $\bar{v}$), since the ocean response to the intraseasonal wind forcing peaks at 90 days and 30–105 day periods could cover the majority of oceanic intraseasonal signals in the Indian Ocean (Han, 2005; Chen et al., 2018). $\tilde{\rho} = \rho - \rho_b$, $\tilde{\rho}' = \tilde{\rho} - \bar{\tilde{\rho}}$. Likewise, $\tilde{\rho}'$ denotes the deviations from the running mean of $\bar{\tilde{\rho}}$. ρ_b and $\bar{\rho}_\theta$ are the background density and potential density averaged from 2000 to 2019. For the barotropic (baroclinic) conversion terms, positive values of T4 (T2) indicate that kinetic (potential) energy is converted from mean flow into eddies, whereas negative values illustrate that the eddy energy is fed back to mean flow.

Additionally, the EKE is also impacted by the pressure work (PW), advection (ADV), wind stress work (WW), and friction (DIFF), as well as T4 (Ivchenko et al., 1997; Geng et al., 2018). These terms are defined as follows:

$$\mathrm{PW} = - -\frac{1}{\rho}\left(u'\frac{\partial P'}{\partial x} + v'\frac{\partial P'}{\partial y} + w'\frac{\partial P'}{\partial z}\right) \tag{5}$$

$$\mathrm{ADV} = -\left(u\frac{\partial\,\mathrm{EKE}}{\partial x} + v\frac{\partial\,\mathrm{EKE}}{\partial y} + w\frac{\partial\,\mathrm{EKE}}{\partial z}\right) \tag{6}$$

$$\mathrm{WW} = \frac{1}{\rho}\left(u_0'\tau_x' + v_0'\tau_y'\right) \tag{7}$$

$$\mathrm{DIFF} = u'\frac{\partial}{\partial z}\left(K_M\frac{\partial u'}{\partial z}\right) + u'F_x' + v'\frac{\partial}{\partial z}\left(K_M\frac{\partial v'}{\partial z}\right) + v'F_y' \tag{8}$$

Since the eddy diffusivity coefficient is complex to obtain accurately, here, we only consider the PW, ADV, and WW terms. In the above equations, P', τ_x' (τ_y'), and u_0' (v_0') indicate the deviations from the running mean of water pressure, wind stresses, and ocean surface velocities, respectively. w is the vertical velocity diagnosed from the continuity equation, and w' is calculated similarly as u'.

To explore the spatial distributions of eddy energy terms, EKE, EPE, T4, T2, PW, and ADV are averaged from the surface to 200m depth, because the seasonal and intraseasonal exchanges of eddy energy mainly happen in the upper ocean.

3 Results

3.1 Seasonal variation of eddy kinetic energy and eddy potential energy

To begin, the seasonal characteristics of EKE and EPE are inspected first. As shown in Figure 2, the distribution of EKE is closely associated with the seasonal counter currents induced by the monsoonal winds in the AS, whereas the variability of EKE has both seasonal and intraseasonal features in the BOB. For EPE, the distribution patterns are similar to EKE, but the magnitude is smaller. Generally, large EKE/EPE can be spotted in six regions, including the SC region (A1 region, marked in Figure 2A), the Gulf of Aden (A2 region), the Laccadive Sea (A3 region), the east of Sri Lanka (B1 region), the EICC region (B2 region), and the northwest of Sumatra (B3 region).

In the AS, strong eddy energy emerges in the SC region during the summer monsoon under the drive of northward SC, which is concluded by previous studies (Chen et al., 2014; Zhan et al., 2020). The largest EKE/EPE locates in the GW region, and the large energy region gradually proceeds northward with the moving GW. By averaging from the surface to 200 m over the designated regions, the monthly mean EKE and EPE are estimated. In the SC region, both EKE and EPE are dramatically large from July to October (Figure 3A), which are greater than 0.11 and 0.05 $m^2 \cdot s^{-2}$ during this period. After the GW collides with Socotra Island, a few new eddies generate in the north part (Akuetevi et al., 2016), which may propagate into

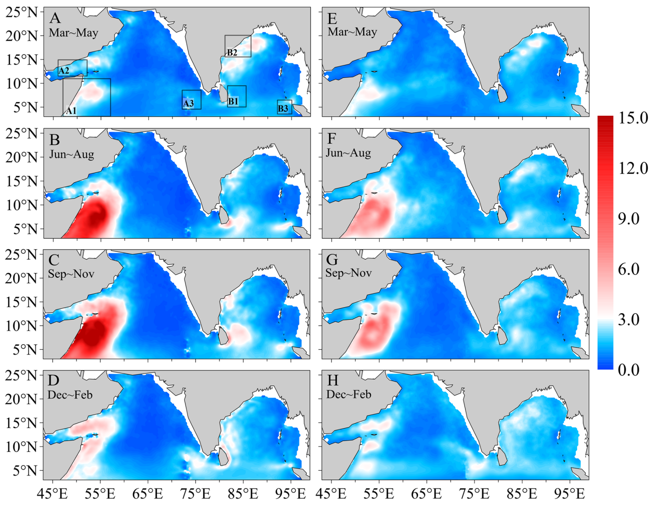

FIGURE 2
Seasonal distribution of eddy kinetic energy (EKE) **(A-D)** and eddy potential energy (EPE) **(E-H)** averaged from the surface to 200 m in spring (March–May), summer (June–August), autumn (September–November), and winter (December–February) (unit: 10^{-2} $m^2 \cdot s^{-2}$). The representative regions are marked as rectangles, including A1 (47°–57°E, 3°–11°N), A2 (46°–52°E, 11.5°–15°N), and A3 (72°–76°E, 4.5°–8.5°N) regions in the Arabian Sea and B1 (81.5°–85.5°E, 5°–9.5°N), B2 (81°–86.5°E, 15.5°–20°N), and B3 (92°–95°E, 3.5°–6.5°N) regions in the Bay of Bengal.

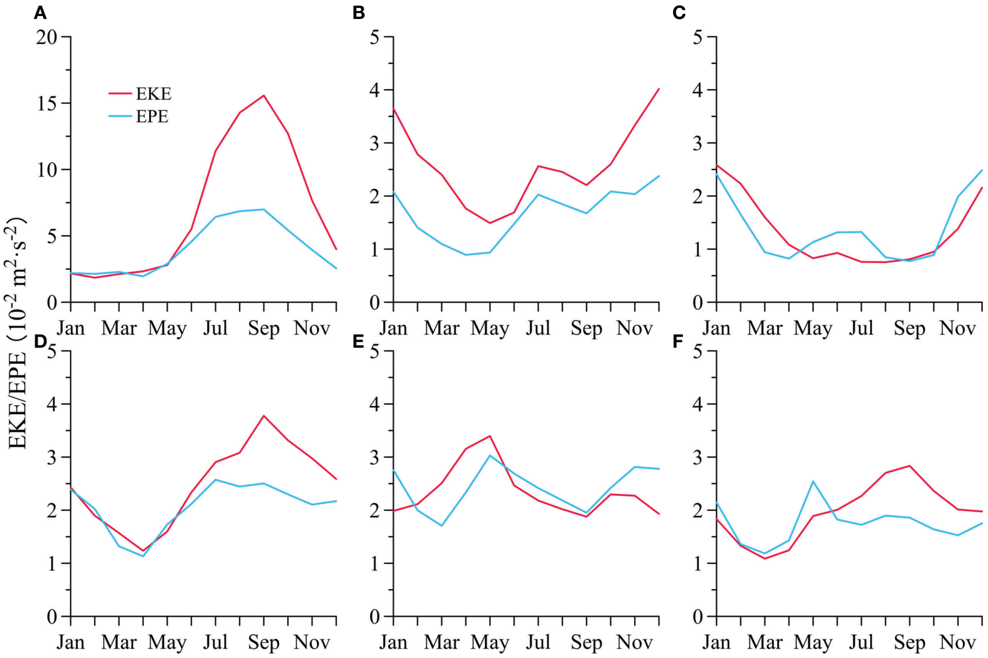

FIGURE 3
Monthly variation of eddy kinetic energy (EKE) and eddy potential energy (EPE) averaged in the A1 **(A)**, A2 **(B)**, A3 **(C)**, B1 **(D)**, B2 **(E)**, and B3 **(F)** regions.

the Gulf of Aden and thus enhance the eddy energy. The southwestward EAC and westward propagating Rossby waves are able to propel eddies into the Gulf of Aden (Al Saafani et al., 2007), resulting in larger eddy energy from October to January. The maximal EKE and EPE occur in December, with peak values of 0.04 and 0.024 m^2·s^{-2}, respectively (Figure 3B). Comparatively, eddy energy is small in the middle of AS throughout the year. In the BOB, large eddy energy occurs to the east of Sri Lanka from June to January, with EKE (EPE) larger than 0.023 m^2·s^{-2} (0.021) during this period (Figure 3D). According to the study by Chen et al. (2018), the oceanic internal instabilities account for 90% contribution in this region. Moreover, the second downwelling coastal Kelvin waves triggered by the equatorial wind forcing also have slight effects, taking up the residual 10% contribution (Rao et al., 2010; Chen et al., 2018). After arriving at the east of Sri Lanka in November, the downwelling coastal Kelvin waves are further intensified by the local wind stress (Suresh et al., 2016), and then the Kelvin waves propagate across the southern tip of India under the drive of the Northeast Monsoon Current, which enhances the eddy energy in the Laccadive Sea, together with the instabilities induced by the low-density water from the BOB, causing a higher EKE (EPE) of 0.026 m^2·s^{-2} (0.025) in January (December) (Figure 3C). In the EICC region, eddy energy is influenced by both oceanic internal instabilities and wind forcing, which contribute to 79% and 21% efficacies, respectively (Chen et al., 2018). Since the EICC is more intense from March to May (Schott and McCreary, 2001), the maximum EKE and EPE both occur in May, which are 0.034 and 0.03 m^2·s^{-2}, respectively (Figure 3E). Unlike the east of Sri Lanka and the EICC region where oceanic internal instabilities dominate, the local and equatorial wind forcings are crucial at the northwest of Sumatra, which account for 22% and 29% contributions of eddy energy, respectively (Chen et al., 2018). Specifically, the Ekman pumping induced by the local wind forcing is prominent in autumn, whereas the reflected Kelvin waves caused by the equatorial wind forcing are predominant in winter (Chen et al., 2018). As a result, the EKE is larger from July to December with a maximum value in September (0.028 m^2·s^{-2}) (Figure 3F).

Moreover, the vertical structures of EKE and EPE are further studied in the six regions (Figure 4). For all of the regions, EKE decreases rapidly in the upper ocean with maximum value at the surface. The surface EKE of the A1 region could exceed 0.18 m^2·s^{-2} in summer, whereas surface EKE mostly varies within 0.08 m^2·s^{-2} for the other regions. The decreasing trends of EKE slow down below 200 m depth, and the seasonal signals could reach 1,000 m depth. The large EPE also lies above 200 m, and the profiles usually have two peaks: one locates near the surface, the other one situates at about 100 m depth, which are primarily induced by the large density deviations ($\tilde{\rho}'$) near the surface and in the thermocline.

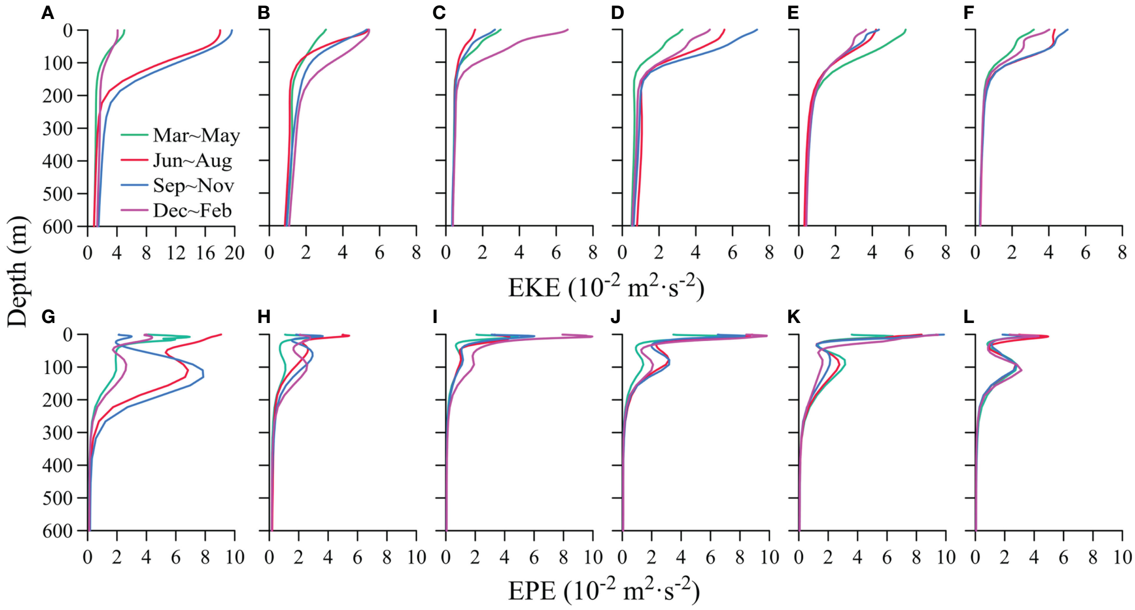

FIGURE 4
Seasonal profiles of eddy kinetic energy (EKE) **(A-F)** and eddy potential energy (EPE) **(G-L)** averaged in the A1, A2, A3, B1, B2, and B3 regions.

3.2 Barotropic and baroclinic conversions

The seasonal energy exchanges between eddy and mean current flow are evaluated from the barotropic and baroclinic conversions. As depicted in Figures 5A-H, the barotropic and baroclinic active regions are closely in accordance with the large EKE/EPE areas, revealing remarkable variability at the west part of the two basins.

Affected by the enormous horizontal velocity shear and density gradient, the strongest barotropic and baroclinic conversions occur in the SC region, showing positive T4 and T2 from June to October, which illustrate that the energy of the mean flow is converted into eddies during the summer monsoon. Meanwhile, some negative bands adjoin the positive regions, indicating that the eddy energy is dissipated to the mean flow simultaneously. To explore the eddy energy conversions in

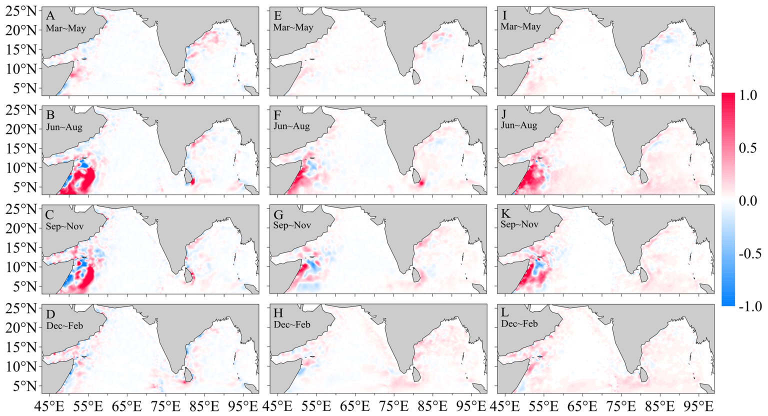

FIGURE 5
Seasonal distribution of T4 **(A-D)** and T2 **(E-H)** and energy conversion between eddy potential energy (EPE) and eddy kinetic energy (EKE) **(I-L)** averaged from the surface to 200 m in spring, summer, autumn, and winter (unit: 10^{-7} m^2·s^{-3}).

detail, the monthly variations of four (two) terms in T4 (T2) averaged above 200 m are analyzed in the six regions (Figure 6). In general, the first and fourth terms of T4 have larger magnitudes, and they exhibit inverse effects most of the time. Contrastively, the second and third terms of T4 are smaller, since positive and negative $u'v'$ are more likely to cancel each other when calculating the regional average value. For the T2, the dominant term varies in different months and regions. In the SC region, the first (fourth) term of T4 dominates the positive (negative) values (Figure 6A), which depend on the zonal gradient of $\bar{u}$ ($\partial\bar{u}/\partial x$) and the meridional gradient of $\bar{v}$ ($\partial\bar{v}/\partial y$), as the $u'u'$ and $v'v'$ are constantly positive. Under the drive of SC and GW, the mean current field is clockwise during the summer monsoon. Thus, the $\partial\bar{u}/\partial x$ ($\partial\bar{v}/\partial y$) is negative (positive) along the west boundary (Figures 7C, G), and yet it is positive (negative) in the southeast part of the SC region. Since the velocity is larger along the west boundary, the sign of region average value is determined by $\partial\bar{u}/\partial x$ and $\partial\bar{v}/\partial y$ along the west boundary. Consequently, the regional mean first (fourth) term is positive (negative). In the equation of T2, $\partial\bar{\rho}_\theta/\partial z$ is less than zero, resulting in negative $-g/(-\rho(\partial\bar{\rho}_\theta/\partial z))$. The velocity anomalies (u' and v'), the zonal and meridional gradients of $\bar{\tilde{\rho}}$ ($\partial\bar{\tilde{\rho}}/\partial x$ and $\partial\bar{\tilde{\rho}}/\partial y$), and the density anomaly ($\tilde{\rho}'$) determine the sign of the two terms in T2 together. During the summer monsoon, the SC and anticyclonic GW enhance the current velocity along the west boundary, causing positive u' and v'. Moreover, the SC brings low-density water northward, and the downwelling caused by the anticyclonic current field also reduces the density in the upper ocean, so $\tilde{\rho}'$ is negative in the SC region. Due to the low density in the center of the GW region, $\partial\bar{\tilde{\rho}}/\partial x$ ($\partial\bar{\tilde{\rho}}/\partial y$) is negative (positive) along the boundary (Figures 7K, O). Combining the above variables, the first (second) term of T2 is negative (positive) eventually. In the Gulf of Aden, T4/T2 is larger from July to January, indicating that the eddy energy exchange is more active after the summer monsoon. Since the southwestward current velocity is faster along the north gulf during the winter monsoon, which will cause positive $\partial\bar{u}/\partial x$ and negative $\partial\bar{v}/\partial y$ (Figures 7D, H), and subsequently lead to the larger negative first term and positive fourth term of T4 from October to December (Figure 6B) . For T2, the two terms have larger magnitudes from October to January, but the positive first term is partially canceled by the negative second term. Actually, the positive T2 is larger from July to August, since the low-density water driving northward by the SC intrudes into the south part of the gulf, which raises the $\partial\bar{\tilde{\rho}}/\partial y$ (Figure 7O) and enhances the second term of T2. In the Laccadive region, the barotropic and baroclinic conversions are stronger during the winter monsoon. The positive fourth term is slightly larger than the negative first term, leading to a positive T4 in January (Figure 6C). Driving by the Northeast Monsoon Current, the low-density water from BOB amplifies the $\partial\bar{\tilde{\rho}}/\partial y$ (Figure 7M), which subsequently enhances the second term of T2 from December to February.

In the BOB, pronounced T4/T2 can be detected in the EICC region. The barotropic conversion is stronger from March to

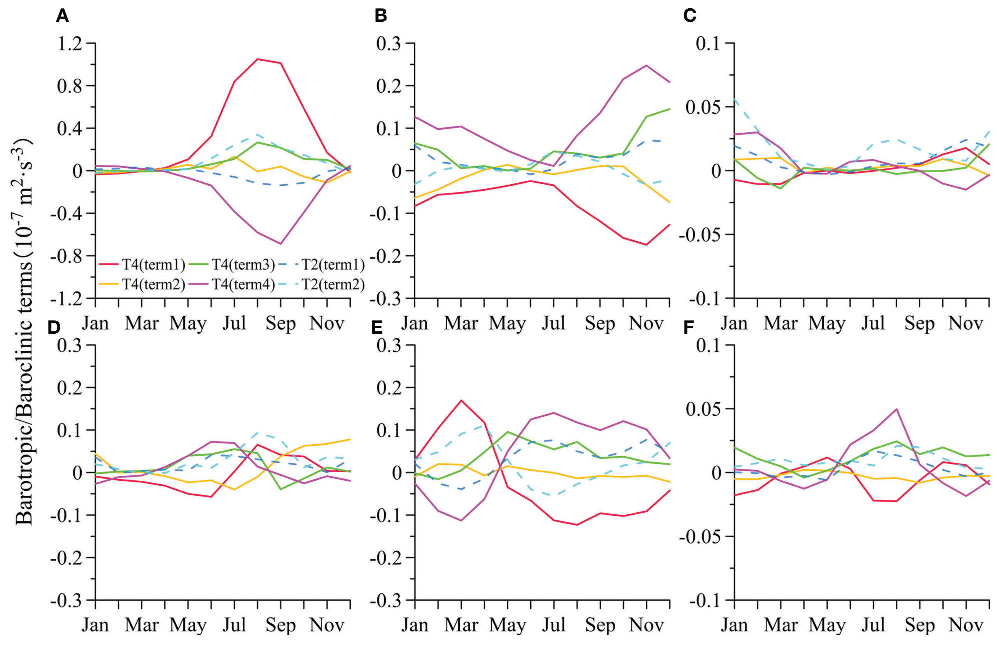

FIGURE 6
Monthly variation of the four terms in T4 and the two terms in T2 averaged in the A1 **(A)**, A2 **(B)**, A3 **(C)**, B1 **(D)**, B2 **(E)**, and B3 **(F)** regions.

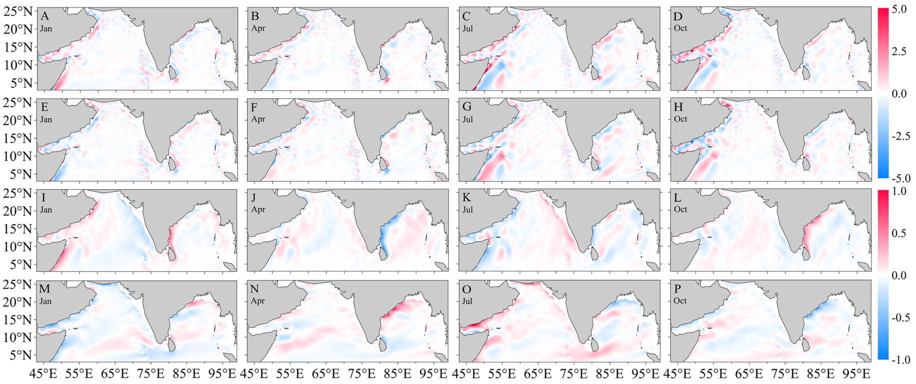

FIGURE 7

The distribution of $\partial\bar{u}/\partial x$ **(A-D)** and $\partial\bar{v}/\partial y$ **(E-H)** in January, April, July, and October (unit: 10^{-6} s^{-1}); the distribution of $\partial\bar{\tilde{\rho}}/\partial x$ **(I-L)** and $\partial\bar{\tilde{\rho}}/\partial y$ **(M-P)** in January, April, July, and October (unit: 10^{-5} kg·m^{-4}).

May, whereas the baroclinic conversion is larger from October to December. As the EICC gradually weakens after April, the first term of T4 turns negative (Figure 6E), which is affected by the $\partial\bar{u}/\partial x$ that changes from negative to positive along the east coast of Orissa (Figures 7B, C). Moreover, the first term is nearly offset by the fourth term, so the positive T4 is attributed to the third term from April to June. Similarly, the two terms of T2 also change the sign after May. The second term of T2 is larger from December to April, whereas the first term regulates the positive value from June to November. To the east of Sri Lanka, positive T4/T2 mainly exists from June to September as the onset of the Southwest Monsoon Current. The third and fourth terms lead the positive T4 from May to July, whereas positive T4 is dominated by the second term after September (Figure 6D). For the T2, the second term is larger from July to September, illustrating that the $\partial\bar{\tilde{\rho}}/\partial y$ is more significant during this period (Figure 7O). At the northwest of Sumatra, positive barotropic conversion occurs from June to September, which is led by the third and fourth terms of T4 (Figure 6F). The baroclinic conversion is larger from July to September, and the two terms of T2 are both positive during this stage.

In line with the EKE/EPE, the barotropic and baroclinic conversions mainly occur above 200 m. In the A1 region, the T4 peaks at the surface, with a maximum value of 2.1×10^{-7} m^2·s^{-3} during the summer monsoon (Figure 8A), which is significantly larger than that of the other regions. The large T2 mainly exists around 150 m in summer and autumn (Figure 8G), producing more EPE in the thermocline (Figure 4G). In the A2 region, surface T4 is positive in summer, but it shifts to negative at about 20 m depth (Figure 8B), which may be induced by the velocity shear beneath the surface. In contrast, the upper ocean T4 is mainly positive in the other seasons. The T2 is larger at the surface during the summer monsoon, while positive T2 is more evident at 100 m depth in autumn and winter (Figure 8H). In the A3 region, the T4 and T2 mainly lie above 100 m with larger values in winter (Figures 8C, I). In the B1 region, the upper ocean T4 is positive except for spring (Figure 8D). In the B2 region, the positive T4 dominates in the upper ocean in spring, summer, and autumn (Figure 8E). In the B3 region, the upper ocean T4 is relatively larger during the summer monsoon (Figure 8F). For the profiles of T2 in the B1, B2, and B3 regions, positive values dominate the upper ocean with larger values near the surface (Figures 8J–L).

It is worth noting that the upper ocean T4 of the B1 region is negative in spring (Figure 8D); however, the corresponding EKE still has considerable value (Figure 4D), which might be directly converted from EPE. Thus, the energy conversion between EPE and EKE is further inspected following the studies of Kang and Curchitser (2015) and Yan et al. (2019). The equation is as follows:

$$\mathrm{EPE} \leftrightarrow \mathrm{EKE} = -g\tilde{\rho}'w'/\rho \tag{9}$$

The energy conversion between EPE and EKE has similar distribution with T2 in the north Indian Ocean (Figures 5I-L), which is in agreement with previous studies (Von Storch et al., 2012; Chen et al., 2014; Kang and Curchitser, 2015; Yan et al., 2019), implying that the two processes happen almost synchronously. Therefore, the transition from mean potential energy to EKE can be considered as two steps: firstly, the available potential energy of the mean flow is converted to EPE, and then EPE releases its energy to EKE *via* vertical density flux.

Vertically, the energy conversions between EPE and EKE mainly happen above 200 m with peak values near the surface or in the thermocline (Figures 8M-R). In the six regions, EPE is generally converted into EKE, showing positive values in the

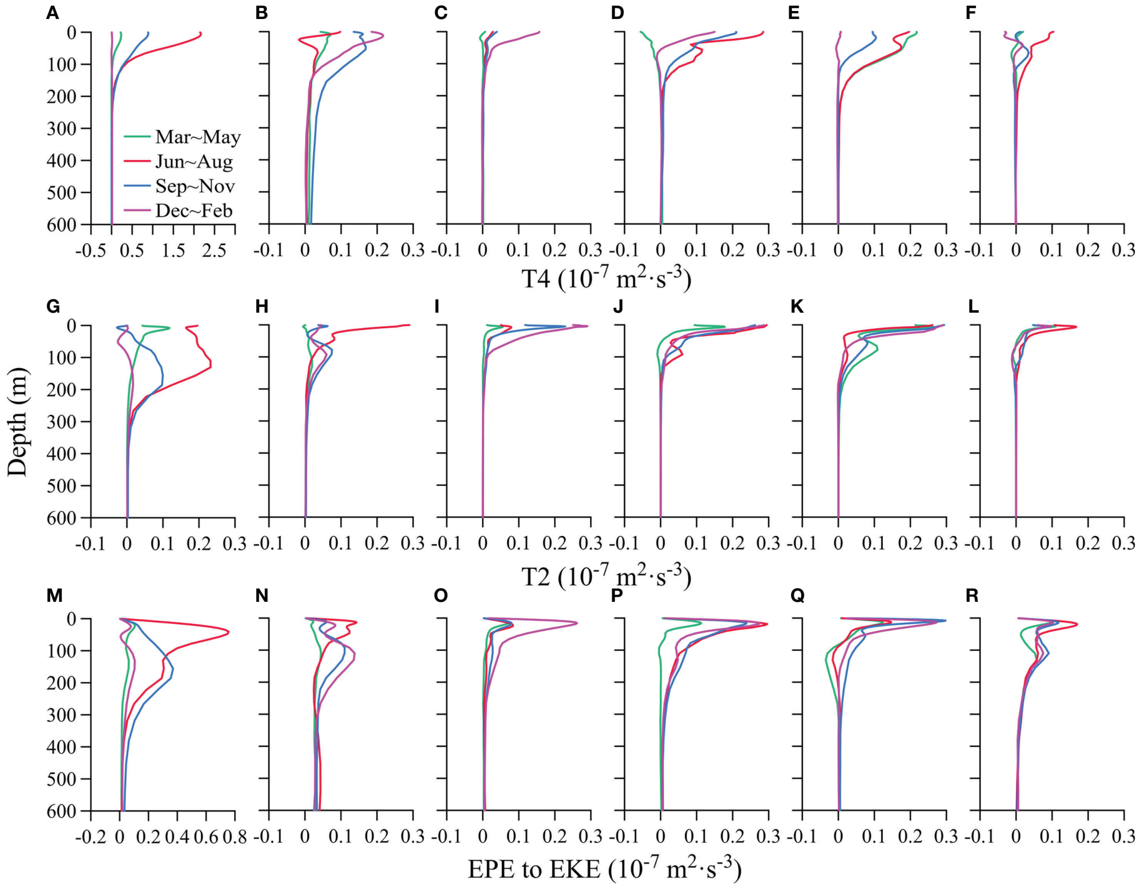

FIGURE 8
Seasonal profiles of T4 **(A-F)** and T2 **(G-L)** and energy conversion between eddy potential energy (EPE) and eddy kinetic energy (EKE) **(M-R)** averaged in the A1, A2, A3, B1, B2, and B3 regions.

upper ocean. As for the B1 region, the kinetic energy from EPE is essential to sustain the EKE during the spring intermediate season, as the mean current even drains EKE through barotropic conversion. Moreover, the Laccadive region also obtains more EKE from the EPE than from the kinetic energy of mean flow (Figures 8C, O), since the barotropic conversion is relatively smaller. Likewise, the energy from EPE is also crucial to the EKE supplement of the A2 region in summer and the B2 and B3 regions in winter.

3.3 Horizontal and vertical redistributions of eddy energy

After the EKE generates, it will be redistributed by the PW and ADV in forms of energy fluxes. To investigate the horizontal and vertical redistributions of EKE separately, the first two terms in Equations 5 and 6 are combined to represent the total horizontal EKE redistribution induced by PW and ADV, whereas the third terms in the two equations are merged as the sum of vertical EKE redistribution.

As depicted in Figure 9, positive and negative bands of horizontal eddy energy flux adjoin each other, indicating that the convergence and divergence of EKE happen simultaneously. The amounts of horizontal EKE redistribution depend on the quantity of available EKE, showing larger variabilities in the six representative regions. The most distinct convergence/divergence of EKE occurs in the SC region during the summer monsoon. In accordance with the results of Zhan et al. (2020), intensive divergence emerges along the SC axis with a convergent band adjacent to it. Compared to the horizontal redistribution, the magnitude of vertical EKE redistribution is smaller. Apart from some positive bands in the SC region, the vertical redistributions of EKE are mostly negative, illustrating that EKE is primarily transferred downward through vertical energy flux. The major cause of vertical EKE redistribution is the PW, since the vertical ADV term is very small.

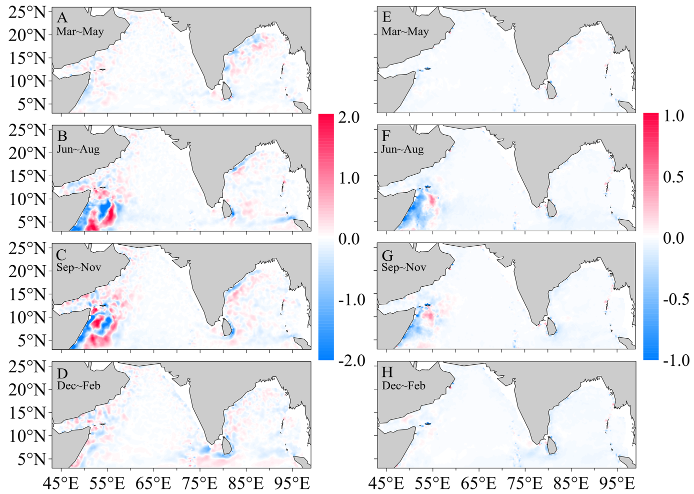

FIGURE 9
Seasonal distribution of horizontal eddy kinetic energy (EKE) redistribution **(A-D)** and vertical EKE redistribution **(E-H)** averaged from the surface to 200 m in spring, summer, autumn, and winter (unit: 10^{-7} $m^2 \cdot s^{-3}$).

The horizontal redistribution of EKE could extend to 1,000 m depth with larger magnitudes above 200 m (Figures 10A-F). In the upper ocean, the PW and ADV both act on the redistribution of EKE, while the effect of PW dominates in the deep ocean, beacause the amounts of EKE for direct ADV decrease with the increment of depth. The profiles of horizontal EKE redistribution mainly reveal negative values during the large EKE seasons, dispersing EKE to the adjacent regions. However, positive values may occur near the surface, implying that EKE is imported from the surrounding areas. The profiles of vertical EKE redistribution are more coincident, exhibiting downward EKE flux in the upper ocean, which is especially stronger near the surface (Figures 10G-L).

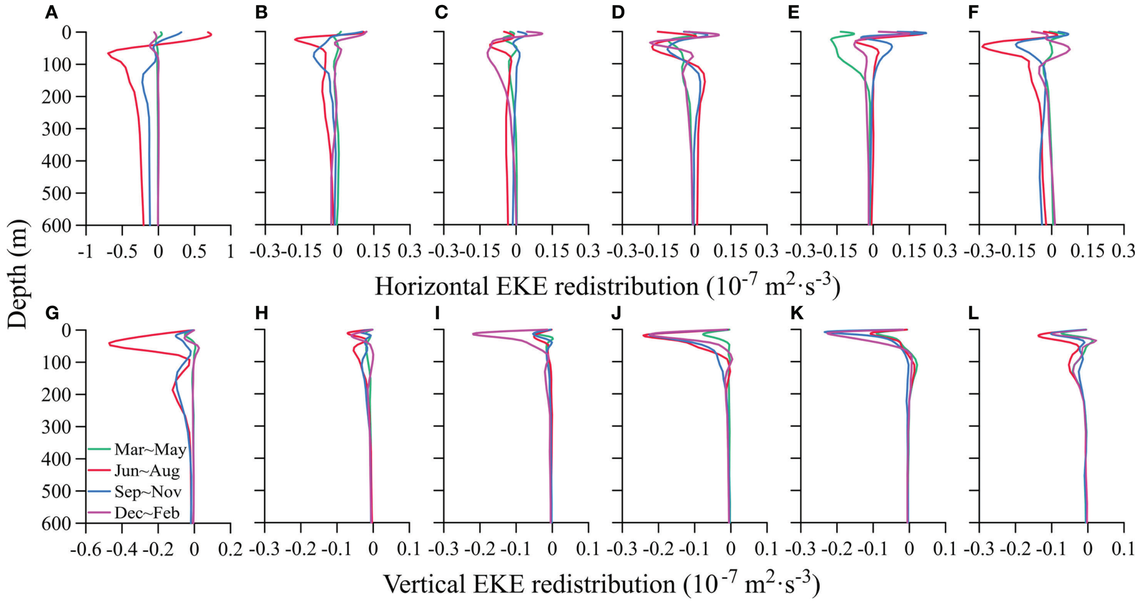

FIGURE 10
Seasonal profiles of horizontal eddy kinetic energy (EKE) redistribution **(A-F)** and vertical EKE redistribution **(G-L)** averaged in the A1, A2, A3, B1, B2, and B3 regions.

3.4 The effect of wind work

The direct wind forcing on EKE can be evaluated by eddy wind work *via* Equation 7. Notably, different choices of surface stress and current can lead to disparate results. When calculating the surface stress, using the relative velocity between 10 m wind and surface current instead of wind speed alone will lower the energy transferring to EKE by wind work (Zhai and Greatbatch, 2007; Seo et al., 2019). Following previous studies (Renault et al., 2016a; Renault et al., 2016b; Yang and Liang, 2018), the geostrophic eddy wind work and mean geostrophic wind work are employed here to estimate the wind energy input. The equations are as follows:

$$\mathrm{WW}_{eg} = \frac{1}{\rho_o}\left(u_g'\tau_x' + v_g'\tau_y'\right) \tag{10}$$

$$\mathrm{WW}_{mg} = \frac{1}{\rho_o}\left(\bar{u}_g\bar{\tau}_x + \bar{v}_g\bar{\tau}_y\right) \tag{11}$$

$$\tau = \rho_a C_D (U_a - U_o)|U_a - U_o| \tag{12}$$

where τ is the surface stress, ρ_a (ρ_o) is the density of air (ocean), C_D is the surface drag coefficient, and U_a (U_o) is the 10 m wind velocity (surface current velocity). $\bar{u}_g$ ($\bar{v}_g$) is the low-frequency background geostrophic surface velocity calculated by 101 days running mean of u_g (v_g), and $u_g^{'}$($v_g^{'}$) represents the corresponding deviation. $\bar{\tau}_x$ ($\bar{\tau}_y$) is low-frequency surface stress calculated by 101 days running mean of τ_x (τ_y), and $\tau_x^{'}$ ($\tau_y^{'}$) represents the deviation. WW_{eg} is the geostrophic eddy wind work, and positive WW_{eg} denotes that the energy is transferred into surface EKE *via* wind forcing. WW_{mg} is the mean geostrophic wind work, and positive WW_{mg} indicates that the wind energy is converted into mean surface kinetic energy.

In accordance with previous studies (Zhai et al., 2012; Xu et al., 2016; Renault et al., 2017), the WW_{eg} primarily dampens eddies, acting as an "eddy killer" that converts EKE to the atmosphere (Figures 11A-D). The dampening effect is stronger during the summer monsoon, especially in the SC region. Yet, the WW_{eg} could enhance the EKE during the spring and autumn intermediate seasons, presenting positive bands along the Somali coast and around the south tip of Sri Lanka. Comparatively, the WW_{mg} could considerably intensify the mean surface kinetic energy, which may further turn into EKE through barotropic conversion. As shown in Figure 11F, intense positive WW_{mg} resides along the Somali coast and around the south tip of Sri Lanka during the summer monsoon, illustrating wind energy input, whereas the coverage and magnitude of positive WW_{mg} dramatically diminish in winter. Moreover, large WW_{mg} can also be spotted in the EICC region, which is consistent with the study of Seo et al. (2019).

4 Summary and discussion

By adopting high-resolution ocean reanalysis data, this study investigates the temporal and spatial characteristics of major eddy energy terms in the north Indian Ocean. The results show that the variabilities of eddy energy terms are strongly affected by the seasonal wind and current, which is particularly evident in six eddy-active regions, including the SC region, the Gulf of Aden, the Laccadive Sea, the east of Sri Lanka, the EICC region, and the northwest of Sumatra.

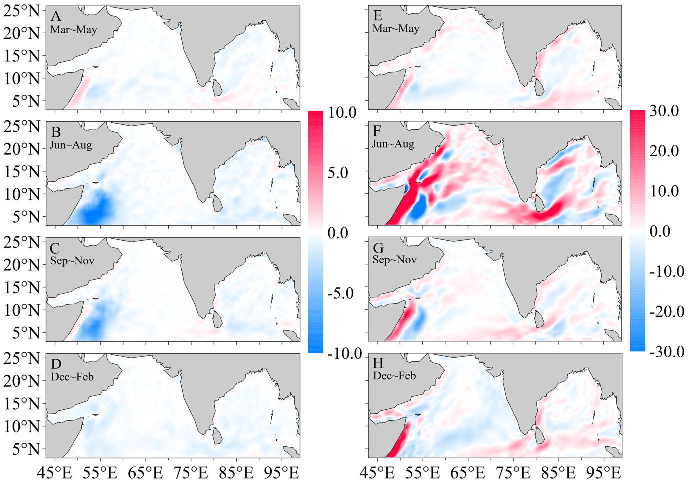

FIGURE 11
Seasonal distribution of WW_{eg} **(A-D)** and WW_{mg} **(E-H)** averaged from the surface to 200 m in spring, summer, autumn, and winter (unit: 10^{-6} $m^3 \cdot s^{-3}$).

As the most energetic region in the north Indian Ocean, the upper ocean EKE (EPE) of the SC region could exceed 0.15 m^2·s^{-2} (0.07) during the summer monsoon. According to Figure 12A, EKE is primarily from the kinetic energy of mean flow, whereas EPE is the secondary EKE source. In the SC region, the oceanic internal instability plays a crucial role in transferring energy from mean flow to eddies. Specifically, the strong velocity of SC enhances EKE through barotropic conversion, while the low-density water brought by the SC amplifies EPE *via* baroclinic conversion, and then the EPE is further converted into EKE by vertical density flux. The horizontal and vertical redistributions of EKE are energy sinks, which vary in sync with the monthly variation of EKE sources, transporting EKE to the adjacent regions or deeper layers. The wind energy input by WW$_{mg}$ is conducive to the increment of mean kinetic energy during the summer monsoon in most regions, while the WW$_{eg}$ exerts a slightly dampening effect to EKE in all of the regions. The annual mean T4, EPE to EKE, horizontal and vertical EKE redistribution, and WW$_{eg}$ are 2.82 × 10^{-8}, 2.02 × 10^{-8}, -0.97 × 10^{-8}, -0.62 × 10^{-8}, and -0.12 × 10^{-8} m^2·s^{-3}, respectively.

Since the southwestward EAC is able to propel eddies into the Gulf of Aden, the eddy activity in the gulf is more significant after the summer monsoon. The EKE is mainly converted from EPE during July to September, whereas the southwestward current generates more EKE *via* barotropic conversion from October to December (Figure 12B). The horizontal and vertical redistributions of EKE have a larger dampening effect from July to September. The annual mean T4, EPE to EKE, horizontal and vertical EKE redistribution, and WW$_{eg}$ are 0.62 × 10^{-8}, 0.68 × 10^{-8}, -0.28 × 10^{-8}, -0.21 × 10^{-8}, and -0.012 × 10^{-8} m^2·s^{-3}, respectively.

In the Laccadive Sea, the energy exchanges are stronger during the two monsoon seasons, especially for the winter monsoon period (Figure 12C). In winter, the Northwest Monsoon Current prevails westward and brings low-density water from the BOB to the AS, enhancing the EPE *via* baroclinic conversion, and then the EPE is converted into EKE through vertical density flux. Moreover, the EPE to EKE of the Laccadive Sea in January has similar magnitude with the value to the east of Sri Lanka in December (Figure 12D), which further implies that the eddy energy of the Laccadive region is related to the low-density water from the BOB. In contrast, the EKE generated *via* barotropic conversion is lesser. The annual mean T4, EPE to EKE, horizontal and vertical EKE redistribution, and WW$_{eg}$ are 0.12 × 10^{-8}, 0.36 × 10^{-8}, -0.27 × 10^{-8}, -0.19 × 10^{-8}, and -0.006×10^{-8} m^2·s^{-3}, respectively.

Due to the instabilities caused by Southwest and Northeast Monsoon Currents, the energy conversions to the east of Sri Lanka

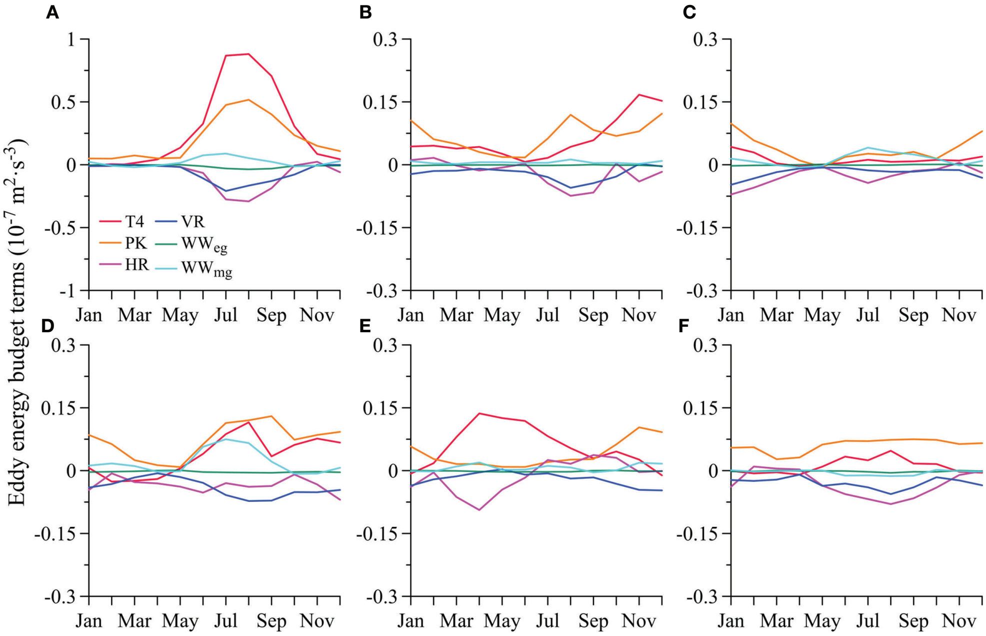

FIGURE 12
Monthly variations of barotropic conversion (T4), eddy potential energy (EPE) to eddy kinetic energy (EKE) (PK), horizontal redistribution of EKE (HR), vertical redistribution of EKE (VR), geostrophic eddy wind work (WW$_{eg}$), and mean geostrophic wind work (WW$_{mg}$) averaged in the A1 **(A)**, A2 **(B)**, A3 **(C)**, B1 **(D)**, B2 **(E)**, and B3 **(F)** regions. (In keeping with the other terms, the WW$_{eg}$ and WW$_{mg}$ are divided by 200, assuming that wind works can be averaged from the surface to 200 m).

are remarkable during the two monsoon seasons. From June to December, EKE generated by barotropic and baroclinic conversions has similar magnitudes (Figure 12D), while EPE is the primary EKE source from January to March. The horizontal and vertical redistributions of EKE also show obvious negative values during the monsoon seasons. The annual mean T4, EPE to EKE, horizontal and vertical EKE redistribution, and WW_{eg} are 0.35×10^{-8}, 0.73×10^{-8}, -0.38×10^{-8}, -0.41×10^{-8}, and -0.028×10^{-8} $m^2 \cdot s^{-3}$, respectively.

In the EICC region, the barotropic conversion caused by strong EICC significantly enhances the EKE from March to June, and the EKE is redistributed by horizontal ADV and PW during this period (Figure 12E). Moreover, the EKE is mainly converted from EPE from October to January, and the vertical redistribution of EKE is the primary EKE sink during this stage. The annual mean T4, EPE to EKE, horizontal and vertical EKE redistribution, and WW_{eg} are 0.58×10^{-8}, 0.39×10^{-8}, -0.19×10^{-8}, -0.21×10^{-8}, and -0.013×10^{-8} $m^2 \cdot s^{-3}$, respectively.

At the northwest of Sumatra, EKE is converted from EPE around the year, whereas the mean current flow mainly produces EKE from June to September (Figure 12F). The horizontal and vertical redistributions of EKE exert a strong dampening effect during the summer monsoon. Unlike the other regions, the WW_{mg} presents a negative effect in summer, implying that the mean kinetic energy is dissipated into wind energy. The annual mean T4, EPE to EKE, horizontal and vertical EKE redistribution, and WW_{eg} are 0.1×10^{-8}, 0.6×10^{-8}, -0.42×10^{-8}, -0.26×10^{-8}, and -0.017×10^{-8} $m^2 \cdot s^{-3}$, respectively.

From the vertical aspect, stronger EKE, EPE, and energy conversions mainly locate above 200 m in the north Indian Ocean. The maximal value of EKE and barotropic conversion mostly occur at the surface, whereas the profiles of EPE and baroclinic conversion may have two peaks, which lie at the surface and in the thermocline. The energy conversion between EPE and EKE has a larger magnitude near the surface. Moreover, the horizontal and vertical redistributions of EKE also have a larger magnitude above 200 m, which transfers upper ocean EKE to ambient region and deeper ocean.

Through this study, we analyze spatial distribution and monthly variation of EKE budget terms in the north Indian Ocean. In the SC region and the EICC region where intense west boundary currents exist, EKE is primarily generated by mean flow *via* barotropic conversion, revealing larger T4 during the strong current periods. For the other regions, the leading source is EPE, which is extracted from the available potential energy of mean flow *via* baroclinic conversion, and then converted into EKE through vertical density flux. After generation, the EKE will be redistributed by the PW and ADV *via* eddy energy flux, and the dampening effects amplify with the increment of EKE. The results of this work provide an overview of eddy energy exchange in the north Indian Ocean; however, we have not examined the eddy energy dissipation induced by friction yet, which shall be discussed in future research.

Data availability statement

Publicly available datasets were analyzed in this study. This data can be found here: the ocean reanalysis data and the surface geostrophic current data is from the Copernicus Marine Environment Monitoring Service (CMEMS) (https://resources.marine.copernicus.eu/). The wind data is from the Remote Sensing Systems (RSS) (https://www.remss.com/measurements/ccmp/).

Author contributions

AZ, XW proposed the conception of the study. BJ conducted the wind work analysis. XZ and LZ contributed to the improvement of the manuscript. CS performed the data analysis and wrote the draft of the manuscript. All authors contributed to the manuscript and approved the submitted version.

Funding

This study is supported by the Key Program of Marine Economy Development Special Foundation of Department of Natural Resources of Guangdong Province (GDNRC [2022]19), the National Natural Science Foundation of China (41976019 and 41906009), the Special Founds for Creative Research (2022C61540).

Conflict of interest

The authors declare that the research was conducted in the absence of any commercial or financial relationships that could be construed as a potential conflict of interest.

Publisher's note

References

Akuetevi, C. Q. C., Barnier, B., Verron, J., Molines, J. M., and Lecointre, A. (2016). Interactions between the Somali current eddies during the summer monsoon: insights from a numerical study. *Ocean Sci.* 12 (1), 185–205. doi: 10.5194/os-12-185-2016

Al Saafani, M. A., Shenoi, S. S. C., Shankar, D., Aparna, M., Kurian, J., Durand, F., et al. (2007). Westward Movement of eddies into the gulf of Aden from the Arabian Sea. *J. Geophys. Res.: Oceans* 112 (C11), 1–12. doi: 10.1029/2006JC004020

Atlas, R., Hoffman, R. N., Ardizzone, J., Leidner, S. M., Jusem, J. C., Smith, D. K., et al. (2011). A cross-calibrated, multiplatform ocean surface wind velocity product for meteorological and oceanographic applications. *Bull. Am. Meteorol. Soc.* 92 (2), 157–174. doi: 10.1175/2010BAMS2946.1

Beal, L. M., and Donohue, K. A. (2013). The great whirl: Observations of its seasonal development and interannual variability. *J. Geophys. Res.: Oceans* 118 (1), 1–13. doi: 10.1029/2012JC008198

Böning, C. W., and Budich, R. G. (1992). Eddy dynamics in a primitive equation model: Sensitivity to horizontal resolution and friction. *J. Phys. Oceanogr.* 22 (4), 361–381. doi: 10.1175/1520-0485(1992)022<0361:EDIAPE>2.0.CO;2

Bruce, J. G., Johnson, D. R., and Kindle, J. C. (1994). Evidence for eddy formation in the eastern Arabian Sea during the northeast monsoon. *J. Geophys. Res.: Oceans* 99 (C4), 7651–7664. doi: 10.1029/94JC00035

Chelton, D. B., Gaube, P., Schlax, M. G., Early, J. J., and Samelson, R. M. (2011a). The influence of nonlinear mesoscale eddies on near-surface oceanic chlorophyll. *Science* 334 (6054), 328–332. doi: 10.1126/science.1208897

Chelton, D. B., Schlax, M. G., and Samelson, R. M. (2011b). Global observations of nonlinear mesoscale eddies. *Prog. Oceanogr.* 91 (2), 167–216. doi: 10.1016/j.pocean.2011.01.002

Chelton, D. B., Schlax, M. G., Samelson, R. M., and de Szoeke, R. A. (2007). Global observations of large oceanic eddies. *Geophys. Res. Lett.* 34 (15), 1–5. doi: 10.1029/2007GL030812

Chen, R., Flierl, G. R., and Wunsch, C. (2014). A description of local and nonlocal eddy-mean flow interaction in a global eddy-permitting state estimate. *J. Phys. Oceanogr.* 44 (9), 2336–2352. doi: 10.1175/JPO-D-14-0009.1

Cheng, X., McCreary, J. P., Qiu, B., Qi, Y., Du, Y., and Chen, X. (2018). Dynamics of eddy generation in the central bay of Bengal. *J. Geophys. Res.: Oceans* 123 (9), 6861–6875. doi: 10.1029/2018JC014100

Cheng, X., Xie, S. P., McCreary, J. P., Qi, Y., and Du, Y. (2013). Intraseasonal variability of sea surface height in the bay of Bengal. *J. Geophys. Res.: Oceans* 118 (2), 816–830. doi: 10.1002/jgrc.20075

Chen, G., Li, Y., Xie, Q., and Wang, D. (2018). Origins of eddy kinetic energy in the bay of Bengal. *J. Geophys. Res.: Oceans* 123 (3), 2097–2115. doi: 10.1002/2017JC013455

Chen, G., Wang, D., and Hou, Y. (2012). The features and interannual variability mechanism of mesoscale eddies in the bay of Bengal. *Continent. Shelf Res.* 47, 178–185. doi: 10.1016/j.csr.2012.07.011

de Marez, C., Carton, X., Corréard, S., l'Hégaret, P., and Morvan, M. (2020). Observations of a deep submesoscale cyclonic vortex in the Arabian Sea. *Geophys. Res. Lett.* 47 (13), 1–10. doi: 10.1029/2020GL087881

Dong, C., McWilliams, J. C., Liu, Y., and Chen, D. (2014). Global heat and salt transports by eddy movement. *Nat. Commun.* 5 (1), 1–6. doi: 10.1038/ncomms4294

Ducet, N., Le Traon, P. Y., and Reverdin, G. (2000). Global high-resolution mapping of ocean circulation from TOPEX/Poseidon and ERS-1 and-2. *J. Geophys. Res.: Oceans* 105 (C8), 19477–19498. doi: 10.1029/2000JC900063

Eden, C., and Böning, C. (2002). Sources of eddy kinetic energy in the Labrador Sea. *J. Phys. Oceanogr.* 32 (12), 3346–3363. doi: 10.1175/1520-0485(2002)032<3346:SOEKEI>2.0.CO;2

Ferrari, R., and Wunsch, C. (2009). Ocean circulation kinetic energy: Reservoirs, sources, and sinks. *Annu. Rev. Fluid Mech* 41 (1), 253–282. doi: 10.1146/annurev.fluid.40.111406.102139

Fischer, J., Schott, F., and Stramma, L. (1996). Currents and transports of the great whirl-socotra gyre system during the summer monsoon. *J. Geophys. Res.: Oceans* 01 (C2), 3573–3587. doi: 10.1029/95JC03617

Fratantoni, D. M., Bower, A. S., Johns, W. E., and Peters, H. (2006). Somali Current rings in the eastern gulf of Aden. *J. Geophys. Res.* 101 (C9), 1–19. doi: 10.1029/2005JC003338

Geng, W., Xie, Q., Chen, G., Liu, Q., and Wang, D. (2018). A three-dimensional modeling study on eddy-mean flow interaction between a Gaussian-type anticyclonic eddy and kuroshio. *J. Oceanogr.* 74 (1), 23–37. doi: 10.1007/s10872-017-0435-z

Gill, A. E., Green, J. S. A., and Simmons, A. J. (1974). Energy partition in the large-scale ocean circulation and the production of mid-ocean eddies, in *Deep sea research and oceanographic abstracts*, vol. 21. (*7*), 499–528. doi: 10.1016/0011-7471(74)90010-2

Han, W. (2005). Origins and dynamics of the 90-day and 30–60-day variations in the equatorial Indian ocean. *J. Phys. Oceanogr.* 35 (5), 708–728. doi: 10.1175/JPO2725.1

Ivchenko, V. O., Tréguier, A. M., and Best, S. E. (1997). A kinetic energy budget and internal instabilities in the fine resolution Antarctic model. *J. Phys. Oceanogr.* 27 (1), 5–22. doi: 10.1175/1520-0485(1997)027<0005:AKEBAI>2.0.CO;2

Jia, F., Wu, L., and Qiu, B. (2011). Seasonal modulation of eddy kinetic energy and its formation mechanism in the southeast Indian ocean. *J. Phys. Oceanogr.* 41 (4), 657–665. doi: 10.1175/2010JPO4436.1

Kang, D., and Curchitser, E. N. (2015). Energetics of eddy–mean flow interactions in the gulf stream region. *J. Phys. Oceanogr.* 45 (4), 1103–1120. doi: 10.1175/JPO-D-14-0200.1

Kuo, Y. C., and Chern, C. S. (2011). Numerical study on the interactions between a mesoscale eddy and a western boundary current. *J. Oceanogr.* 67 (3), 263–272. doi: 10.1007/s10872-011-0026-3

Lellouche, J. M., Greiner, E., Le Galloudec, O., Garric, G., Regnier, C. , Drevillon, M., et al. (2018). Recent updates to the Copernicus marine service global ocean monitoring and forecasting real-time 1/ 12 high-resolution system. *Ocean Sci.* 14 (5), 1093–1126. doi: 10.5194/os-14-1093-2018

Lorenz, E. N. (1955). Available potential energy and the maintenance of the general circulation. *Tellus* 7 (2), 157–167. doi: 10.3402/tellusa.v7i2.8796

Mata, M. M., Wijffels, S. E., Church, J. A., and Tomczak, M. (2006). Eddy shedding and energy conversions in the East Australian current. *J. Geophys. Res.: Oceans* 111 (C9), 1–18. doi: 10.1029/2006JC003592

Mukherjee, A., Chatterjee, A., and Francis, P. A. (2019). Role of Andaman and nicobar islands in eddy formation along western boundary of the bay of Bengal. *Sci. Rep.* 9 (1), 1–10. doi: 10.1038/s41598-019-46542-9

Pirro, A., Fernando, H. J. S., Wijesekera, H. W., Jensen, T. G., Centurioni, L. R., and Jinadasa, S. U. P. (2020). Eddies and currents in the bay of Bengal during summer monsoons. *Deep Sea Res. Part II: Topic. Stud. Oceanogr.* 172, 1–14. doi: 10.1016/j.dsr2.2019.104728

Qiu, B. (1999). Seasonal eddy field modulation of the north pacific subtropical countercurrent: TOPEX/Poseidon observations and theory. *J. Phys. Oceanogr.* 29 (10), 2471–2486. doi: 10.1175/1520-0485(1999)029<2471:SEFMOT>2.0.CO;2

Qiu, B., and Chen, S. (2004). Seasonal modulations in the eddy field of the south pacific ocean. *J. Phys. Oceanogr.* 34 (7), 1515–1527. doi: 10.1175/1520-0485(2004)034<1515:SMITEF>2.0.CO;2

Qiu, C., Liang, H., Sun, X., Mao, H., Wang, D., Yi, Z., et al. (2021). Extreme Sea-surface cooling induced by eddy heat advection during tropical cyclone in the north Western pacific ocean. *Front. Mar. Sci.* 8. doi: 10.3389/fmars.2021.726306

Rao, R. R., Kumar, M. G., Ravichandran, M., Rao, A. R., Gopalakrishna, V. V., and Thadathil, P. (2010). Interannual variability of kelvin wave propagation in the wave guides of the equatorial Indian ocean, the coastal bay of Bengal and the southeastern Arabian Sea during 1993–2006. *Deep Sea Res. Part I: Oceanogr. Res. Pap.* 57 (1), 1–13. doi: 10.1016/j.dsr.2009.10.008

Renault, L., McWilliams, J. C., and Masson, S. (2017). Satellite observations of imprint of oceanic current on wind stress by air-sea coupling. *Sci. Rep.* 7 (1), 1–7. doi: 10.1038/s41598-017-17939-1

Renault, L., Molemaker, M. J., Gula, J., Masson, S., and McWilliams, J. C. (2016b). Control and stabilization of the gulf stream by oceanic current interaction with the atmosphere. *J. Phys. Oceanogr.* 46 (11), 3439–3453. doi: 10.1175/JPO-D-16-0115.1

Renault, L., Molemaker, M. J., McWilliams, J. C., Shchepetkin, A. F., Lemarié, F., Chelton, D., et al. (2016a). Modulation of wind work by oceanic current interaction with the atmosphere. *J. Phys. Oceanogr.* 46 (6), 1685–1704. doi: 10.1175/JPO-D-15-0232.1

Richardson, P. L. (1983). Eddy kinetic energy in the north Atlantic from surface drifters. *J. Geophys. Res.: Oceans* 88 (C7), 4355–4367. doi: 10.1029/JC088iC07p04355

Rieck, J. K., Böning, C. W., Greatbatch, R. J., and Scheinert, M. (2015). Seasonal variability of eddy kinetic energy in a global high-resolution ocean model. *Geophys. Res. Lett.* 42 (21), 9379–9386. doi: 10.1002/2015GL066152

Schott, F. A., and McCreary, J. J.P. (2001). The monsoon circulation of the Indian ocean. *Prog. Oceanogr.* 51 (1), 1–123. doi: 10.1016/S0079-6611(01)00083-0

Seo, H., Subramanian, A. C., Song, H., and Chowdary, J. S. (2019). Coupled effects of ocean current on wind stress in the bay of Bengal: Eddy energetics and upper ocean stratification. *Deep Sea Res. Part II: Topic. Stud. Oceanogr.* 168, 1–14. doi: 10.1016/j.dsr2.2019.07.005

Shankar, D., and Shetye, S. R. (1997). On the dynamics of the Lakshadweep high and low in the southeastern Arabian Sea. *J. Geophys. Res.: Oceans* 102 (C6), 12551–12562. doi: 10.1029/97JC00465

Shankar, D., Vinayachandran, P. N., and Unnikrishnan, A. S. (2002). The monsoon currents in the north Indian ocean. *Prog. Oceanogr.* 52 (1), 63–120. doi: 10.1016/S0079-6611(02)00024-1

Stammer, D., and Wunsch, C. (1999). Temporal changes in eddy energy of the oceans. *Deep Sea Res. Part II: Topic. Stud. Oceanogr.* 46 (1-2), 77–108. doi: 10.1016/S0967-0645(98)00106-4

Suresh, I., Vialard, J., Izumo, T., Lengaigne, M., Han, W., McCreary, J., et al. (2016). Dominant role of winds near Sri Lanka in driving seasonal sea level variations along the west coast of India. *Geophys. Res. Lett.* 43 (13), 7028–7035. doi: 10.1002/2016GL069976

Uchida, T., Abernathey, R., and Smith, S. (2017). Seasonality of eddy kinetic energy in an eddy permitting global climate model. *Ocean Model.* 118, 41–58. doi: 10.1016/j.ocemod.2017.08.006

Venaille, A., Vallis, G. K., and Smith, K. S. (2011). Baroclinic turbulence in the ocean: Analysis with primitive equation and quasigeostrophic simulations. *J. Phys. Oceanogr.* 41 (9), 1605–1623. doi: 10.1175/JPO-D-10-05021.1

Verezemskaya, P., Barnier, B., Gulev, S. K., Gladyshev, S., Molines, J. M., Gladyshev, V., et al. (2021). Assessing eddying (1/12°) ocean reanalysis GLORYS12 using the 14-yr instrumental record from 59.5° n section in the Atlantic. *J. Geophys. Res.: Oceans* 126 (6), 1–22. doi: 10.1029/2020JC016317

Vic, C., Roullet, G., Carton, X., and Capet, X. (2014). Mesoscale dynamics in the Arabian Sea and a focus on the great whirl life cycle: A numerical investigation using ROMS. *J. Geophys. Res.: Oceans* 119 (9), 6422–6443. doi: 10.1002/2014JC009857

Von Storch, J. S., Eden, C., Fast, I., Haak, H., Hernández-Deckers, D., Maier-Reimer, E., et al. (2012). An estimate of the Lorenz energy cycle for the world ocean based on the STORM/NCEP simulation. *J. Phys. Oceanogr.* 42 (12), 2185–2205. doi: 10.1175/JPO-D-12-079.1

Wentz, F. J., Scott, J., Hoffman, R., Leidner, M., Atlas, R., and Ardizzone, J. (2015). *Remote sensing systems cross-calibrated multi-platform (CCMP) 6-hourly ocean vector wind analysis product on 0.25 deg grid, version 2.0* (Santa Rosa, CA: Remote Sensing Systems).

Wyrtki, K., Magaard, L., and Hager, J. (1976). Eddy energy in the oceans. *J. Geophys. Res.* 81 (15), 2641–2646. doi: 10.1029/JC081i015p02641

Xu, C., Zhai, X., and Shang, X. D. (2016). Work done by atmospheric winds on mesoscale ocean eddies. *Geophys. Res. Lett.* 43 (23), 12–174. doi: 10.1002/2016GL071275

Yang, C., Bricaud, C., Drevillon, M., Storto, A., Bellucci, A., and Santoleri, R. (2022). The role of eddies in the north Atlantic decadal variability. *Front. Mar. Sci.* 9. doi: 10.3389/fmars.2022.781788

Yang, Y., and San Liang, X. (2018). On the seasonal eddy variability in the kuroshio extension. *J. Phys. Oceanogr.* 48 (8), 1675–1689. doi: 10.1175/JPO-D-18-0058.1

Yan, X., Kang, D., Curchitser, E. N., and Pang, C. (2019). Energetics of eddy–mean flow interactions along the western boundary currents in the north pacific. *J. Phys. Oceanogr.* 49 (3), 789–810. doi: 10.1175/JPO-D-18-0201.1

Zhai, X., and Greatbatch, R. J. (2007). Wind work in a model of the northwest Atlantic ocean. *Geophys. Res. Lett.* 34 (4), 1–4. doi: 10.1029/2006GL028907

Zhai, X., Greatbatch, R. J., and Kohlmann, J. D. (2008). On the seasonal variability of eddy kinetic energy in the gulf stream region. *Geophys. Res. Lett.* 35 (24), 1–6. doi: 10.1029/2008GL036412

Zhai, X., Johnson, H. L., and Marshall, D. P. (2010). Significant sink of ocean-eddy energy near western boundaries. *Nat. Geosci.* 3 (9), 608–612. doi: 10.1038/ngeo943

Zhai, X., Johnson, H. L., Marshall, D. P., and Wunsch, C. (2012). On the wind power input to the ocean general circulation. *J. Phys. Oceanogr.* 42 (8), 1357–1365. doi: 10.1175/JPO-D-12-09.1

Zhan, P., Guo, D., and Hoteit, I. (2020). Eddy-induced transport and kinetic energy budget in the Arabian Sea. *Geophys. Res. Lett.* 47 (23), 1–11. doi: 10.1029/2020GL090490

Zhang, Z., Wang, W., and Qiu, B. (2014). Oceanic mass transport by mesoscale eddies. *Science* 345 (6194), 322–324. doi: 10.1126/science.125241

Zhou, J., Zhou, G., Liu, H., Li, Z., and Cheng, X. (2021). Mesoscale eddy-induced ocean dynamic and thermodynamic anomalies in the north pacific. *Front. Mar. Sci.* 8. doi: 10.3389/fmars.2021.756918

Zu, Y., Fang, Y., Sun, S., Yang, G., Gao, L., Duan, Y., et al. (2022). The seasonality of mesoscale eddy intensity in the southeastern tropical Indian ocean. *Front. Mar. Sci.* 9. doi: 10.3389/fmars.2022.855832